



# **Water Resources Research**

## RESEARCH ARTICLE

10.1002/2016WR020293

#### **Kev Points:**

- · A new inversion method is presented, using a transdimensional algorithm to reconstruct fracture network geometries
- Tracer tomography is used to obtain information about the fractured media
- The method is applied to a 2-D hypothetical example and a hypothetical example modeled after a fracture distribution from the field

#### **Supporting Information:**

• Supporting Information S1

### **Correspondence to:**

M. Somogyvári. somogyvari@erdw.ethz.ch

#### Citation:

Somogyvári, M., M. Jalali, S. Jimenez Parras, and P. Bayer (2017), Synthetic fracture network characterization with transdimensional inversion, Water Resour. Res., 53, 5104-5123, doi:10.1002/2016WR020293.

Received 19 DEC 2016 Accepted 31 MAY 2017 Accepted article online 7 JUN 2017 Published online 26 JUN 2017

# Synthetic fracture network characterization with transdimensional inversion

Márk Somogyvári¹, Mohammadreza Jalali¹, Santos Jimenez Parras¹ 📵, and Peter Bayer¹,² 📵



<sup>1</sup>Department of Earth Sciences, ETH Zurich, Zurich, Switzerland, <sup>2</sup>Institute for New Energy Systems (InES), Technische Hochschule Ingolstadt, Ingolstadt, Germany

**Abstract** Fracture network geometry is crucial for transport in hard rock aquifers, but it can only be approximated in models. While fracture orientation, spacing, and intensity can be obtained from borehole logs, core images, and outcrops, the characterization of in situ fracture network geometry requires the interpretation of spatially distributed hydraulic and transport experiments. In this study, we present a novel concept using a transdimensional inversion method (reversible jump Markov Chain Monte Carlo, rjMCMC) to invert a two-dimensional cross-well discrete fracture network (DFN) geometry from tracer tomography experiments. The conservative tracer transport is modeled via a fast finite difference model neglecting matrix diffusion. The proposed DFN inversion method iteratively evolves DFN variants by geometry updates to fit the observed tomographic data evaluated by the Metropolis-Hastings-Green acceptance criteria. A main feature is the varying dimensions of the inverse problem, which allows for the calibration of fracture geometries and numbers. This delivers an ensemble of thousands of DFN realizations that can be utilized for probabilistic identification of fractures in the aquifer. In the presented hypothetical and outcrop-based case studies, cross sections between boreholes are investigated. The procedure successfully identifies major transport pathways in the investigated domain and explores equally probable DFN realizations, which are analyzed in fracture probability maps and by multidimensional scaling.

### 1. Introduction

Simulation of flow and transport in fractured rocks means dealing with highly structured systems with significant permeability contrasts, pronounced preferential flow paths, and characteristic anisotropies in the hydraulic parameters. Realistic reconstruction of fracture networks in numerical models is a challenge, which is commonly restricted by the limited amount of data and insufficient insight from field measurements [Berkowitz, 2002; Neuman, 2005; Illman, 2014]. To get around these restrictions, concepts with reduced model complexity or with focus on relevant features such as a few prominent fractures are applied. Through these, estimation of model parameters can be simplified, and inversion problems are better posed.

Equivalent continuum models [Illman and Neuman, 2003; Sahimi, 2011] and stochastic continuum models [Day-Lewis et al., 2000; Vesselinov et al., 2001a, 2001b; Hao et al., 2008; Illman et al., 2009; Zha et al., 2015], for example, approximate the fractured rock as a smoothened and highly heterogeneous porous medium and are able to delineate the main flow channels in an aquifer. These models are mostly limited to fracture networks which have a high fracture density [Long et al., 1982], and where flow channeling plays an important role [Sahimi, 2011]. They cannot directly incorporate crucial structural information such as statistics on main fracture orientations or intensity. However, smoothening of discrete fractures allows for the use of established geostatistical space-filling methods, which are convenient for computationally efficient model inversion [Yeh et al., 1996; Franssen and Gómez-Hernández, 2002; Schöniger et al., 2012; Illman et al., 2015]. Together with the use of data sets obtained from spatially distributed field measurements, well-constrained flow and transport models can be derived.

Spatially distributed measurements are fundamental to invasive tomographic tests such as hydraulic, pneumatic, and tracer tomography [Martinez-Landa and Carrera, 2006; Illman et al., 2009; Berg and Illman, 2011; Hu et al., 2015; Paradis et al., 2015; Zhou et al., 2016]. Here, pressure or tracer signals are recorded between different sources and receivers (e.g., multiple well screens) and the data are inverted to image the spatial heterogeneity in the subsurface. Illman [2014] reviewed the state-of-the art in hydraulic and pneumatic

© 2017. American Geophysical Union. All Rights Reserved.

tomography in fractured rock, with successful applications to synthetic models [Hao et al., 2008; Ni and Yeh, 2008; Zha et al., 2016], laboratory [Sharmeen et al., 2012], and field cases [Meier et al., 2001; Vesselinov et al., 2001a, 2001b; Franssen and Gómez-Hernández, 2002; Brauchler et al., 2003; Ni and Yeh, 2008; Illman et al., 2009; Castagna et al., 2011; Zha et al., 2015, 2016]. All these applications utilize continuum models, which are calibrated based on volume-averaging multi-Gaussian geostatistical models, or utilizing smoothing regularization [Brauchler et al., 2003]. Shortcomings are not only the limited realism of the models, but also continuum assumptions may yield unsatisfactory calibration of the hydraulic parameters, such as described in the work of Sharmeen et al. [2012]. Here, hydraulic conductivity of the rock matrix was overestimated, which is considered a consequence of treating the fractured rock as a single continuum, or in other words, a result of underestimating the conductivity of fractures.

Discrete fracture networks (DFN) are realistic mappings of fracture geometries based on the field observation via a stochastic representation of fracture properties. Individual fracture geometry and fracture network connectivity are among the key parameters for such a realistic representation [Hestir et al., 1998, 2001; Jang et al., 2008; Frampton and Cvetkovic, 2010; Niven and Deutsch, 2012; Dorn et al., 2013; Li et al., 2014]. DFN models could model flow and transport in fractured media, although the strong reliance on the cubic law makes these simulations very sensitive to aperture estimations [Neuman, 1988, 2005]. Still, DFN models could better represent the fractured media than continuum models if the number of fractures is small. As a basis for DFN construction, statistical information of the fractured rock (such as fracture intensity) can be used, which is hard to exploit in continuum models. In field cases, however, this requires implementing highly parameterized fracture networks, which are difficult to adjust to hydraulic measurements. The biggest challenge of calibrating DFNs is the high number of parameters that would be required for individual tuning of each fracture. This is complicated by the expected nonconvexity of the inverse problem, by insufficient data for unique model calibration, and by the need for flexible automatic network implementation in the numerical model during iterative calibration. For example, any change in the number of fractures within a DFN during the inversion process results in a change in the number of model parameters, making it impossible to use traditional optimization techniques.

Available automated calibration procedures could commonly reduce the dimension and complexity of inverse problems. For instance, *Mauldon et al.* [1993] and *Datta-Gupta et al.* [1995] simulated the fracture network via partially connected conductors with equal or variable apertures, aligned to a predefined lattice as a finite element approximation of the fractured system. Other concepts keep the number of fractures fixed while adjusting their hydraulic properties [*Le Borgne et al.*, 2007; *Le Goc et al.*, 2010; *Dorn et al.*, 2013; *Klepikova et al.*, 2014], activating-deactivating fractures [*Hestir et al.*, 1998; *Niven and Deutsch*, 2012], or solving the problem over the statistical parameters of the DFN but not on the exact geometries [*Jang et al.*, 2008]. [*Dorn et al.*, 2013] suggested that using variable dimension DFN inversion would be a good choice to improve the capabilities of the existing DFN-based inversion techniques.

In this study we follow the suggestion by *Dorn et al.* [2013] and propose a new methodology that uses transdimensional Bayesian inversion [*Green*, 1995] to reconstruct the geometry of DFN models. This enables us to not only adjust the fracture geometries but also the number of fractures during the inversion procedure. Fracture network geometry is among the challenging properties to determine between boreholes. As prior information, statistical data available for fractured rocks are utilized. By processing data from tomographic measurements, most probable fracture locations and connectivities are identified.

### 2. Methodology

# 2.1. Simulation of Tracer Tomography

Tomographical methods use penetrating signals to obtain information of closed volumes by means of a multisources/multireceivers setup. These set-ups deliver experimental data which, when inverted together, can be utilized to visualize subsurface structures. Tracer tests use injected substances (solutes or particles) or heat to map the pathways of transport in unknown aquifer systems. Conservative tracers do not decay or react with the flowing fluid or with the rock matrix. For tracer tomography, multilevel tracer injection is used (which is obtained by repeated tracer tests or by using multiple tracers at the same time) and the breakthrough curves are recorded at multiple depth points in downgradient wells (receivers) [Illman et al., 2010; Jiménez et al., 2016; Somogyvári et al., 2016]. In fractured media, local injection can be achieved by

1944/9737, 2017, 6, Downloaded from https://agupubs.onlinelibrary.wiley.com/doi/10.10022016WR020293 by Fak-Martin Luther Universitats, Wiley Online Library on [02/07/2024]. See the Terms and Conditions (https://onlinelibrary.wiley.com/ems-and-conditions) on Wiley Online Library for rules of use; OA atticles are governed by the applicable Creative Commons Licenses

using packer systems to isolate specific fractures. The new inversion procedure here is developed relying on virtual tomographic experiments simulated with given DFNs. Such a reference DFN serves as the "truth," which needs to be reconstructed by the inversion procedure. We focus on 2-D models of vertical DFN profiles investigated by tomographic cross-well testing. After simulating conservative tracer injections in one well, the breakthrough curves at the other well represent the observations that are used for calibration.

For forward simulation of the experiments, a fast and robust hydraulic model has been developed to simulate the pressure and tracer propagation inside the fracture network [Jalali, 2013]. This model is based on an implicit finite difference approach and has the capability to solve for both steady state and transient conditions. For simulating the tracer experiments, the steady state solutions are used. Only the fracture network in the domain is discretized and it is assumed that the matrix is impermeable and does not react with the tracer. Tracer diffusion between the fractures and the surrounding rock matrix is neglected [Neretnieks, 1980]. These assumptions are approximate, but appropriate for formations such as crystalline rock. By simulating a vertical cross section between two wells, the thickness of fractures is assumed to be unity (perpendicular to the 2-D DFN plane), and fracture aperture and length control the storativity of each fracture element. Fracture conductivity for each element is calculated using the cubic law, assuming each fracture segment consists of two parallel plates (fracture walls).

Initially, the mass conservation equation for a control volume without any chemical reaction is solved until a steady state condition is satisfied. A constant pressure gradient is applied between the injection and monitoring boreholes and the pressure propagation is calculated using an implicit finite difference method (backward time, centered space method "BTCS"). The 2-D assumption requires the use of pressure boundary conditions, which is considered appropriate in low permeability rocks. The fracture's flow rate is related to the fracture pressure gradient via Darcy's law. The output of this simulation is the pressure and velocity field in the discrete fracture network.

The advection-dispersion equation is then solved for the fracture network as a result of the tracer injection at the source interval. In this case, an implicit and upwind finite difference method is implemented in order to overcome the instabilities introduced by the central differencing scheme after tracer injection initiation as well as at the tracer front. Two reasons can be mentioned for the observed instabilities in the transient advection-dispersion problems: advection dominated flow (i.e., high Peclet number) and sharp gradients during small time steps as a result of transient solution. *Brooks and Hughes* [1982] showed that these instabilities could be overcome using the upwind solution of the differential equations. The forward model will then estimate the concentration field in the fracture network and the tracer breakthrough curves (BTCs) for selected monitoring points in the observation well.

### 2.2. Principles of Transdimensional Inversion

While traditional inversion methods solve inverse problems over a predefined set of parameters [Menke, 1984], transdimensional inversion techniques vary the number of parameters during the inversion process and solve the problem over an a priori unknown number of parameters [Sambridge et al., 2012]. Dealing with an unknown number of parameters increases the complexity of the inverse model. However, this may be compensated by lowering the number of model constraints, and by replacing several independent inverse model runs with different fixed problem dimensions by one transdimensional run. Green [1995] proposed a Bayesian concept of sampling from the posterior probability distribution of a transdimensional inverse problem. This reversible jump Markov Chain Monte Carlo (rjMCMC) method (also known as Metropolis-Hastings-Green (MHG) algorithm) has become the most popular inference method to handle this problem and has also made its way to geosciences. The method has shown to be effective on tomographic problems where the inverse model is defined as a spatial distribution of parameters. Bodin and Sambridge [2009] have proposed an rjMCMC application for seismic tomography and Jiménez et al. [2016] utilized the concept to invert tracer tomography experiments in porous media with pilot points. Mondal et al. [2010] used rjMCMC to resolve porous flow in heterogeneous media and Mardia et al. [2007] employed the method for fractured rock modeling based on the structural data from borehole intersections. Mardia et al. [2007] reveals the suitability of rjMCMC as a flexible plane fitting algorithm to orient fractures in space, assuming that prior knowledge on fracture properties or borehole data are available. Fractures in a DFN model are usually oriented with given statistical properties, and rjMCMC is a probabilistic sampling procedure especially suited for handling parameter distributions. Their approach, however, does not consider

1944/973, 2017, 6, Downloaded from https://agupubs.onlinelibrary.wiley.com/doi/10.1002/2016WR020293 by Fak-Martin Luther Universitats, Wiley Online Library on [02/07/2024]. See the Terms and Conditions (https://onlinelibrary.wiley.com/term

calibration to observations from tomographic experiments. In fact, hydraulic and tracer tomographic measurements provide additional insight and thus have the potential to better reconstruct those fractures relevant for flow and transport. Tomographic experiments for DFN calibration will be considered here.

A Bayesian approach requires that all information is handled as random variables, in the form of probability density functions (PDF). The goal of Bayesian inference is to map the posterior probability distribution of the problem [Gelman et al., 2004]. The posterior probability is determined by the available prior information and the likelihood of the observation data. Using Bayes' theorem, the posterior probability can be written as:

$$P(\theta|\xi) = \frac{P(\xi|\theta)P(\theta)}{P(\xi)} \tag{1}$$

where  $P(\theta|\xi)$  is the posterior probability distribution, the probability of a model parameter set  $(\theta)$  given the observation data  $(\xi)$ .  $P(\xi|\theta)$  is the likelihood function of the observation data, or the probability of observation data  $(\xi)$  given the model parameters  $(\theta)$ .  $P(\theta)$  is the available prior information of the model parameters before observations are made.  $P(\xi)$  is the PDF of the observations. This term is independent from the model parameters, so it can be considered constant throughout the modeling. When the posterior of a problem cannot be expressed in an analytical form, a purpose-built sampling algorithm can be used, such as the rjMCMC method. This perturbs the model parameters and can also vary their number (the dimensionality of the problem).

#### 2.3. DFN Inversion Procedure

Figure 1 depicts the DFN inversion procedure. In this study, the examined model parameters are the geometrical properties of the fractures; i.e., their locations and lengths. For this initial inverse modeling effort, the physical properties of the fractures such as apertures are considered constant and uniform for each fracture set. Our studied reference DFNs are built up by two fracture sets with different inclination angles and apertures, as fractured rocks are often dominated by two fracture sets [Valley, 2007; Ziegler et al., 2015].

The fracture length distribution (FLD) is one of the key statistical properties. In natural rocks, smaller fractures are more frequent than larger ones. A common approximation for this trend on a field scale is to use a power law [*Torabi and Berg*, 2011]. In models, truncated FLDs are used. As very short fracture segments are less relevant for flow and transport [*Bour and Davy*, 1997; *de Dreuzy et al.*, 2002; *Darcel et al.*, 2003; *Baghbanan and Jing*, 2007], they are excluded in our work (see Figure 2b). Fracture intensity is calculated as the total length of fractures over the investigated area [*La Pointe*, 1988]. Additionally, a technical parameter, the discretization length, is defined. It represents the resolution of the forward model, and thus determines the scale of geometric manipulations. Accordingly, in our approach, the DFN models are built up from straight fracture segments, with lengths taken from a discretized FLD. The interconnections between the fractures are also spaced according to the predefined discretization length.

The inversion procedure (Figure 1) is initiated by randomly generating a DFN realization, r, based on given statistical properties. It is implemented in a forward model and evaluated by comparison to the observations. In each subsequent iteration, a new DFN realization is proposed by sequentially updating the geometry of the previous one. The rjMCMC algorithm is reversible by definition [*Green*, 1995]. Reversibility means that the algorithm runs with the same rules backward as forward. This is considered when defining the following three geometry updates: fracture addition, fracture deletion, and fracture shift.

Fracture addition is the so-called birth move of the rjMCMC algorithm, where the dimensionality of the problem is extended and one new fracture is added to the DFN. There are several rules concerning this update. For example, the position of the new fracture is drawn randomly, but not over the whole domain as the added fracture is always connected to the DFNs. This is important to maintain the reversibility of the algorithm. The length of the added fracture is drawn from a prior fracture length distribution (FLD). This FLD is recalculated after each update to guide the actual FLD toward the initially defined FLD. This recalculation is needed, because the fracture deletion update does not obey any FLD rule. Since it draws from the initially defined FLD, it would yield a distorted FLD. The addition update has three substeps (Figures 2a–2c):

1. First, the fracture set and the insertion point are randomly selected (Figure 2a). The predefined discretization length divides each fracture into equal length segments and each segment end represents an

and-conditions) on Wiley Online Library for rules of use; OA articles are governed by the applicable Creative Commons

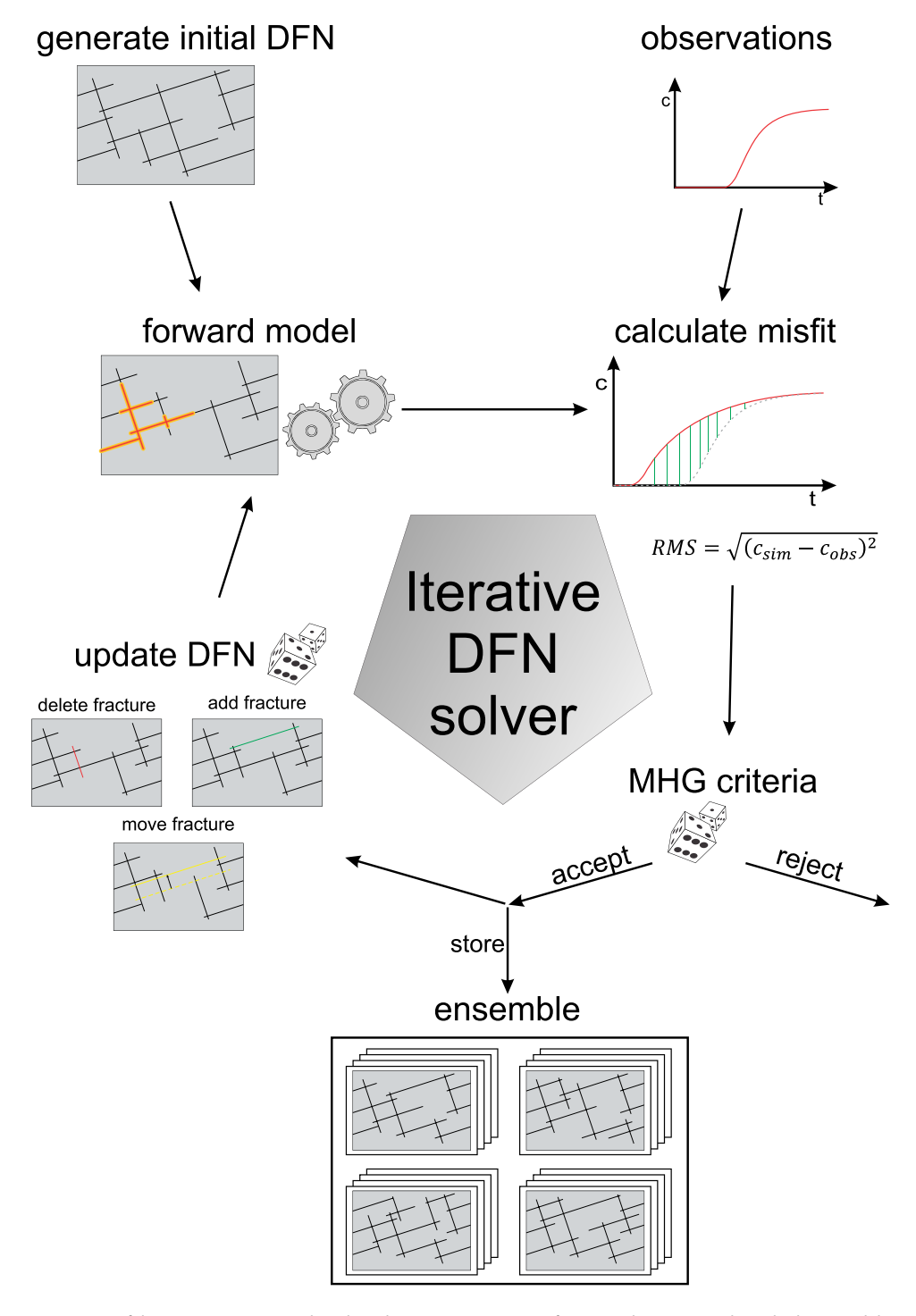


**Figure 1.** Overview of the DFN reconstruction algorithm. The reconstruction starts from a random generated initial solution and the input of the method is the experiment data. The steps of the iterative DFN solver are the following: update DFN model, simulate tomography, calculate misfit, accept, or reject the updated DFN. The accepted DFN realizations are stored in an ensemble, which serve as the output of the algorithm.

insertion point. To avoid fracture overlaps, a fracture can only be added to an insertion point, which is on a fracture from the other fracture set.

2. Second, the length of the inserted fracture is determined (Figure 2b). Each insertion point has a maximum insertable fracture length to avoid overlaps. This is reflected by drawing the fracture length from a truncated FLD.

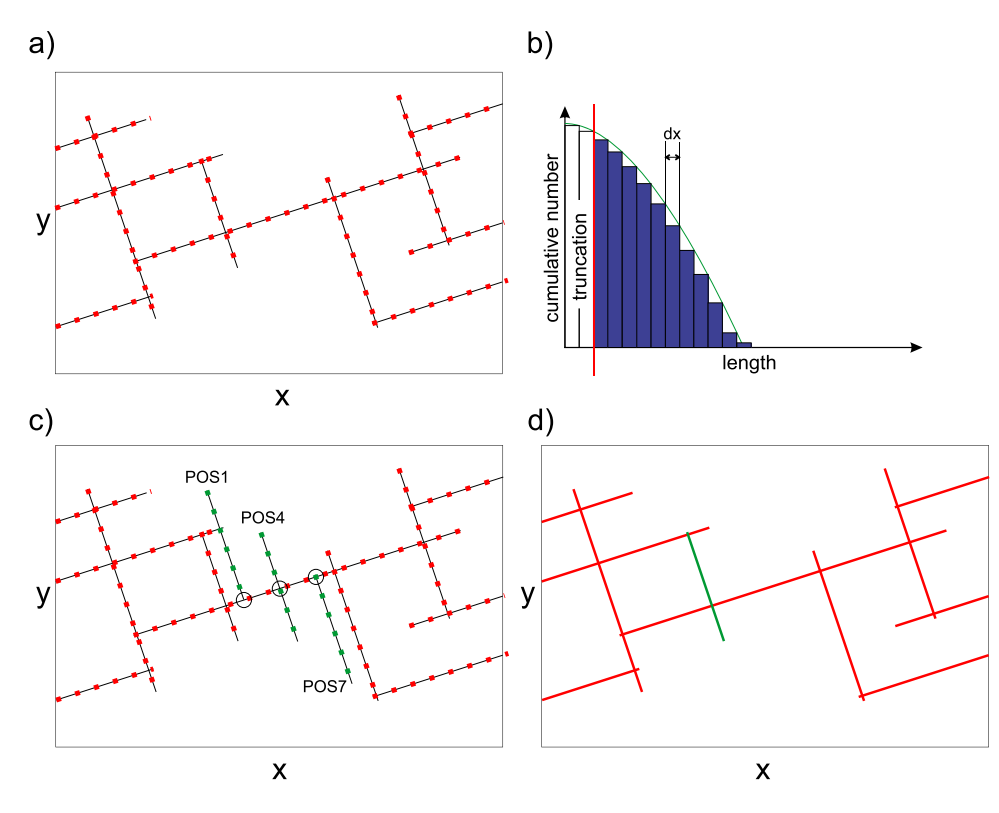


Figure 2. Different update steps of DFN reconstruction. (a) Fracture addition: identify possible insertion points. (b) Fracture addition: draw fracture length from the discretized fracture length distribution (dx: discretization length). (c) Fracture addition: draw the position of the insertion point on the inserted fracture. (d) Fracture deletion: identify deletable fractures (red: nondeletable, green: deletable).

3. The third step is to find the position of the intersection between the new fracture and the insertion point (Figure 2c). The possible positions are constrained by the length of the fracture and also other fractures above and below the inserted fracture from the same set.

Fracture deletion is the so-called death move of the rjMCMC algorithm, when the problem dimensionality is reduced. Before random deletion, the fractures that can be deleted are identified (Figure 2d).

- A fracture cannot be deleted if its deletion would disconnect the sources and receivers of the tomographic experiment in the model, as the forward model can only be executed if all sources and receivers are connected.
- 2. A fracture cannot be deleted if it is not intersecting with any other fractures. Otherwise the reversibility of the algorithm would be violated, as the deleted fracture could not be added back again. An irreversible update could not be evaluated by the rjMCMC algorithm.
- 3. The fractures connecting the source and receiver points to the rest of the DFN are permanent. They cannot be deleted or shifted in order to keep the fracture network connected. The properties of these fractures are considered to be known from borehole measurements prior the tomographic experiment.

Fracture shift is the third possible update. A deletable fracture is shifted along one of its intersecting fractures until the closest free insertion points. The technical implementation of this update is the combination of the earlier two: first deletion and then the insertion of the fracture at another position.

The type of update is randomly selected according to initially defined probabilities. These probabilities do not have to be constant, but they can change from iteration to iteration. If the fracture intensity reaches a minimum limit, the fracture deletion update is disabled. If it reaches a maximum limit, the fracture addition update is disabled. These limits assure that the fracture intensities of the solutions stay close to the predefined value. After an update, the tomographic experiment is simulated with the proposed new DFN realization, r'.

The misfit between the simulations and the observations is calculated to characterize the "goodness" of a DFN realization. Different misfits can be used regarding the type of the experiments and the data quality. In

1944/973, 2017, 6, Downloaded from https://agupubs.onlinelibrary.wiley.com/doi/10.1002/2016WR020293 by Fak-Martin Luther Universitats, Wiley Online Library on [02/07/2024]. See the Terms and Conditions (https://onlinelibrary.wiley.com/etms-and-conditions) on Wiley Online Library for rules of use; OA articles are governed by the applicable Creative Commons

1944/7973, 2017, 6, Downloaded from https://agupubs.onlinelibrary.wiley.com/doi/10.1002/2016WR020293 by Fak-Martin Luther Universitats, Wiley Online Library on [02/07/2024]. See the Terms and Conditions (https://onlinelibrary.wiley

this study, the misfit is oriented at the root mean squared (RMS) error between the simulated and the observed measurements for the same source-receiver combination. It is also possible to use moments or breakthrough times for comparison instead of the full curve in this step. This could be advantageous when the quality of the breakthrough curves is poor or the flow field is altered by the used tracer (e.g., density effects [Somogyvári et al., 2016]).

The rjMCMC evaluates the proposed DFN realization using the Metropolis Hastings Green (MHG) acceptance criterion [*Green*, 1995]. The MHG criterion,  $\alpha(r'|r)$ , combines the evolution of the misfit with the statistical properties of the proposed update:

$$\alpha(r'|r) = \min[1, \text{prior ratio} \times \text{likelihood ratio} \times \text{proposal ratio} \times \text{Jacobian}]$$
 (2)

$$\alpha(r|rI) = \min \left[ 1, \frac{p(rI)}{p(r)} \times \frac{p(\xi|rI)}{p(\xi|rI)} \times \frac{q(r|rI)}{q(rI|rI)} \times |II| \right]$$
(3)

where r is the i-th realization, r' is the updated realization (proposal), p(r) is the PDF of the prior,  $p(\xi|r)$  is the likelihood function, q(r'|r) is the proposal probability, and J is the Jacobian.

The MHG criterion makes it possible to compare realizations with different numbers of parameters by not only comparing the likelihoods, but also the reversible updates. The likelihood function of a simulated measurement quantifies the probability of the observations given a realization of parameters. Since the noise of the measurements typically follows a normal distribution, the likelihood function reads as a Gaussian function:

$$p(\xi|r) = \frac{1}{\sqrt{4\pi\sigma^2}} \exp\left(-\frac{(\xi - \xi(r))^2}{2\sigma^2}\right) \tag{4}$$

which is equivalent to using a RMS misfit [Aster et al., 2013]. The variance of the simulated data noise ( $\sigma^2$ ) defines the acceptance rate of the rjMCMC algorithm. The variance of the likelihood function is set as the noise of the observations [Gelman et al., 2004; Geyer, 2011].

The proposal ratio is the ratio between the probability of the reverse step (q(r|r)) and the forward step (q(r'|r)). The updates have to be reversible; otherwise, the reverse step probability cannot be calculated. The proposal ratio makes it possible to compare realizations with different parametrization, by defining the transient step probabilities between them.

Each proposal probability is built up from the probabilities of the substeps of the used update (see Figure 2). For fracture addition, the proposal probability can be expressed as:

$$P(addition) = P(insertion_{point}) \times P(length|points) \times P(position|length \& points)$$
(5)

$$P(addition) = \frac{1}{count(points)} \times FLD_{truncated} \times \frac{1}{possible\ positions}$$
 (6)

First, the probability of selecting one insertion point is calculated from the total number of possible insertion points. Then the probability of the drawn injection length is calculated from the FLD and truncated to the fracture length limits at the given insertion points. Finally, the probability of the fracture positioning is calculated as well (also limited by the DFN). The reverse update of the fracture addition is the fracture deletion:

$$P(deletion) = \frac{1}{count(deleteable\_fractures)}$$
 (7)

The probability of fracture deletion is calculated from the number of deletable fractures in the realization. In the case of a fracture shift, the proposal ratio is 1. Regarding the prior ratio of the MHG criterion, only noninformative priors are used for the updates in this study (e.g., FLD). These priors are considered within the proposal ratio calculation and thus the prior ratio is always one [Aster et al., 2013].

For the evaluation of the MHG ratio ( $\alpha$ ), a random number  $\beta$  is drawn from a uniform distribution between 0 and 1. The proposal is accepted if  $\beta \leq \alpha$  and rejected if  $\beta > \alpha$ . Accepted realizations are stored, and

use; OA articles are governed by the applicable Creative Commons Licens

together serve as the result ensemble. The new iteration is started with the last accepted DFN realization. Rejected realizations are discarded.

### 2.4. Implementation

The used initial DFN solution is generated randomly based on the given statistical parameters (FLD, spacing, fracture intensity) and it needs to connect sources and receivers. In order to reach this, a very dense DFN is generated by repeated additions until the domain is completely filled with fractures (when no free insertion points exist). From this point, randomly selected fractures are chosen and deleted when the two wells remain connected. This is continued until the desired fracture intensity value is reached. To maintain a homogeneous distribution of fractures over the whole domain, the fracture intensity is calculated over smaller subareas by dividing the domain into quadrants and further if needed. This homogeneity is important, because prior the calibration we consider the given value of fracture intensity valid over the whole investigated domain. The obtained realization is the initial solution for the inversion procedure (Figure 1).

The convergence rate of the algorithm depends on the chosen variance value of the likelihood function. If this value was set too low, the process does not converge. In this case, the algorithm does not accept any update when the misfit would increase. This would trap the algorithm in the first reached local minimum of the inverse problem [Aster et al., 2013]. The optimal value of likelihood variance is case specific; a good choice is to use the variance value of the measurements, which is a common solution for conventional Markov chain applications [Gelman et al., 2004].

The rjMCMC algorithm requires a great number of iterations in order to map the posterior of the inverse problem properly. The convergence of Markov chains can be divided into two phases. The first phase is when the misfit is rapidly converging to zero (or to a minimal value). This is called the burn in phase [Geyer, 2011]. The accepted realizations of this phase are not stored because they are strongly dependent on the used initial DFN realization. In the second phase, the misfits of the accepted realizations converge with small fluctuations around a stable value. Ideally, samples from this second phase serve as equally probable solutions to the inverse problem. The sequentially produced realizations have small differences because each accepted iteration has been created by one update. To properly map the posterior probability of the inverse problem with these small steps, a large number of samples is required (typically over 10,000 accepted realizations).

The computational time of each iteration is dominated by the computational time for the forward model. Clearly, consideration of further processes such as matrix diffusion would increase the computational burden. Even if our forward model is fast and allows flexible adjustment of fracture geometries, alternative implementations such as mesh-free fracture models appear well suited [Noetinger et al., 2016]. The calculation speed of the forward model used here correlates with the number of fractures. Forward models with a large number of fractures would reduce the computational efficiency. This is modulated by truncation of the FLD, and thus by avoiding small hydraulically inactive fractures. The other time consuming process is to identify which fracture can be deleted without splitting the connection between the source-receiver points. This requires repeated connection tests after deleting one by one all the fractures within the DFN. We improved this process by parallelizing it to multiple threads (according to the used CPU architecture).

## 3. Test Cases

Two example cases are investigated with the presented DFN inversion. The fracture network of the first case is a hypothetical variant with simple geometry. The second synthetic geometry is created based on an outcrop field data. With both fracture networks, tracer tomography experiments are simulated and the fracture network geometry in the vertical cross section between source and receiver well is reconstructed.

# 3.1. Simple Hypothetical Case

In this case, two wells on the left and right model boundaries are connected by one main fracture (Figure 3a). It belongs to the first of two fracture sets, with inclinations of 10° and 110°, and apertures of 3 and 2 mm, respectively. In each of the wells, three source or receiver-points are connected to the aquifer via fixed fractures that belong to the same set as the main fracture of the model. Keeping these fractures fixed assumes that they have been localized and described through preliminary borehole geophysical investigation. An initially uniform pressure of 200 kPa is applied to the model domain. In order to duplicate

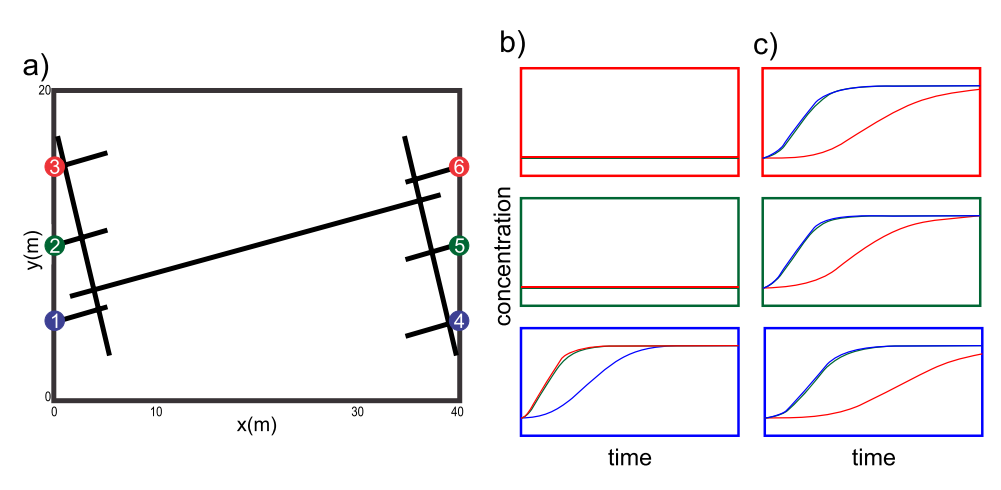


**Figure 3.** (a) Synthetic fracture network model. Injection and observation points are marked as numbered and colored dots. (b) Tracer breakthrough curves (normalized by injection concentration) for tomography to the right direction (left well: injections, right well: observations). The color of the frame matches with the injection point color, while the color of the curves matches with the observation point color. (c) Tracer breakthrough curves of the opposing experiment.

the recorded data, each well serves for injection and observation. An injection pressure of 300 kPa is assigned to the injection interval of the one well, and the pressure of the other production well is set to 100 kPa. The simulation of tracer transport starts only after the steady state flow field is established. Tracer concentrations in the fractures are initially zero. Continuous tracer injection is started at time t=0 using a 20 mg/L solution of an ideal conservative tracer. The tracer injection is maintained until the end of the experiment. The end of the experiment is set where complete breakthroughs are detected in every observation point (except where no breakthrough occurred). The used experimental time was 200 s and concentrations were measured every 10 s. Here, 10% Gaussian noise is added to the simulated observations to represent measurement noise. The dispersion coefficient for the tracer is  $D=0.6 \text{ m}^2\text{s}^{-1}$ . Every injection is simulated as an independent experiment, starting from a tracer-free state. In practice, however, this could be performed as a multitracer experiment with simultaneous injections of different types of tracers [e.g., *Jiménez et al.*, 2016].

### 3.2. Outcrop-Based Case

In addition to the simple hypothetical case, flow and transport in a mapped fracture network is simulated. It stems from the Tschingelmad outcrop from the upper Aar valley in the Grimsel region of the Central Alps, Switzerland [see Ziegler et al., 2013, 2014, for detailed geological description of the fractured rocks in the area] (Figure 4a). The fractured system is hosted in the granite rocks of the central Aar Massif. A 50 m imes50 m outcrop surface area is selected, where the identified fractures form two loosely connected zones. Two fracture sets are identified based on the distribution of their inclinations, and different apertures of 1.5 and 0.5 mm are assigned according to typical values reported from the Grimsel region [Bossart and Mazurek, 1991]. The FLD of the fracture network roughly follows the expected power law [Torabi and Berg, 2011], which is truncated and fractures smaller than 1 m are ignored in the model (Figure 4c). Equivalent to the hypothetical case, three sources and three receiver points are used, located at the right and left edge of the domain at known fracture ends. The same initial and boundary conditions are used as in the previous case, but the experiment is only performed in one direction without swapping the injection and observation well, which is considered to be a more realistic scenario [Doro et al., 2015; Djibrilla Saley et al., 2016; Jiménez et al., 2016]. The experimental time was set to 2000 s and the concentrations were measured every 20 s. Given the longer time of the experiment, much more data points are collected than in the hypothetical case.

### 4. Result Processing

### 4.1. Ensemble Size

The termination criterion of transdimensional Markov chain algorithms is an open question because convergence diagnostic techniques used in conventional MCMC simulations are not applicable for transdimensional cases [Bodin and Sambridge, 2009]. Our solution to overcome this problem is based on the

1944/973, 2017, 6, Downloaded from https://agupubs.onlinelibrary.wiley.com/doi/10.1002/2016WR020293 by Fak-Martin Luther Universitats, Wiley Online Library on [02/07/2024]. See the Terms and Conditions (https://onlinelibrary.wiley.com/etms-and-conditions) on Wiley Online Library for rules of use; OA articles are governed by the applicable Creative Commons

19447973, 2017, 6, Downloaded from https://agupubs.

elibray.wiley.com/doi/10.1002/2016WR020293 by Fak-Martin Luther Universitats, Wiley Online Library on [02/07/2024]. See the Terms and Conditions (https://onlinelibrary.wiley.com/ter

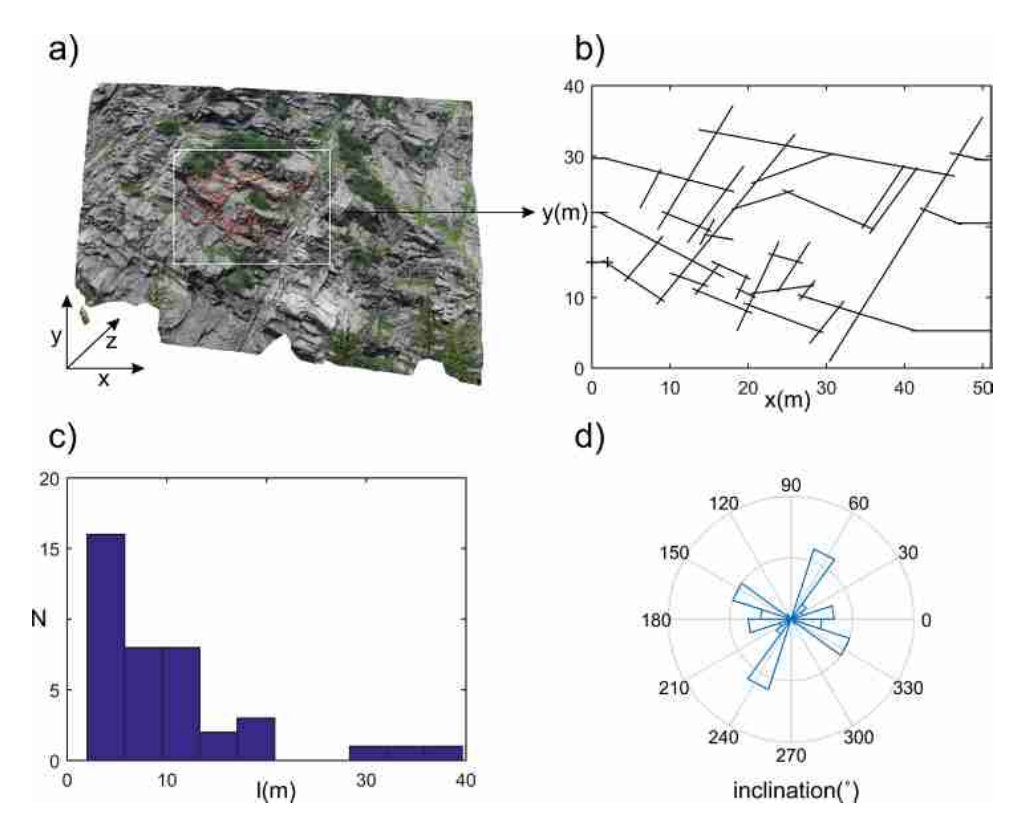


Figure 4. Outcrop-based model (a) 3-D surface model of the Tschingelmad outcrop, (b) identified 2-D DFN geometry, (c) fracture length distribution of DFN (N: cumulative number, I: fracture length), and (d) fracture angle distribution of DFN.

suggestions of [Gelman et al., 2004]. They check the distribution of the parameter vector in the ensemble and if it is not converged to a common distribution, they continue the inversion until the length of the Markov chain is doubled. Our approach is conceptually similar, but without the possibility to examine parameter distributions, we investigated if the result (fracture probability map and multidimensional scaling) shows any major changes (changes in the dominant transport pathways) if the chain length is extended (double the size of the ensemble). If the two results are similar, this means that the posterior of the inverse problem is already sampled by the first part of the sequence and latter sequence parts are just sampling from the same realizations again. If the two results are different, the inversion is continued and the same conditions are checked with a longer sequence.

DFN realizations from the beginning of the chain are considered part of the burn-in phase. The endpoint of the burn-in phase is identified after the visual inspection of the evolution of the misfits, where the values are converged [Jiménez et al., 2016]. To minimize the influence from the burn-in phase, the length of the discarded sequence is doubled.

The DFN inversion produces a large number (more than 10,000) of DFN realizations, which is called ensemble. Instead of a complete presentation of all of the realizations, we concentrate on the statistical information from the ensemble. In the realizations, each fracture is represented by three inverted parameters (two coordinates and the length), the models contain hundreds of fractures, and the number of fractures can vary. Therefore, individual analysis of inverted parameters is not done here, but two different ways to visualize the full ensemble results are suggested in the following.

### 4.2. Fracture Probability Map

The most straightforward way of result visualization is to plot exemplary DFN realizations from the ensemble. This can be misleading, since many fractures in the realizations are not used for tracer transport, and they appear as relics without influence on the inversion. The fractures where transport takes place are the hydraulically active fractures, and the inversion process is only sensitive to their positions, but not to those of the rest. The active fractures of a DFN realization are those where changes in the tracer concentration is

-conditions) on Wiley Online Library for rules of use; OA articles are governed by the applicable Creative Commons

measureable during the simulation. In order to visualize the results of an ensemble of realizations, a map showing the probability of hydraulically active fractures is chosen. This fracture probability map is generated by stacking many DFN realizations together, ideally all results from the ensemble. However, due to the large ensemble size and huge number of parameters, with many similar realizations, a subset is used to represent the mapped posterior distribution. This sample is generated by keeping only every *k*-th realization of the ensemble, which is known as sequence thinning [*Gelman et al.*, 2004]. Local probabilities are calculated after rasterizing each realization and computing the frequency with which a fracture is found in each pixel in the ensemble.

### 4.3. Multidimensional Scaling

Instead of local fracture probabilities, a clustering technique is used to discriminate among characteristic DFN geometries identified in the results ensemble. This is accomplished by multidimensional scaling (MDS), which visualizes similarities and differences among DFN realizations by projecting their relative distances into a Euclidian space [Borg and Groenen, 2005]. For this, the DFN realizations are rasterized similarly as for calculation of fracture probability maps. Then these rasterized realizations are compared to each other in pairs, cell-by-cell, to calculate the relative differences among them. We call these differences realization distances. All the calculated DFN realization distances are stored in one distance matrix, where matrix element (i,j) is the distance between the i-th and the j-th realization. The distance matrix stores the relation between all the investigated DFN realizations.

As the distances among the realizations are relative measurements rather than absolute indicators of fracture geometry, they can only be visualized directly in a multidimensional space. The MDS method is designed to project these multidimensional point clouds into an *N*-dimensional space, with minimal distortion on the distances between the points [*Caers et al.*, 2010]. We use the classical MDS technique to project the distance matrix to a 2-D Euclidian plane. The distance matrix does not contain any absolute location of the samples, just their relative position to each other. Thus, the axes of the MDS projected point cloud do not contain any relevant information, and the projection only shows the relations among the different realizations. The point cloud can be used for clustering in order to identify representative DFN realizations within the ensemble with significant differences. Alternatively, to choose a representative realization, fracture probability maps can also visualize the subset of realizations within a cluster.

### 5. Results

# 5.1. Hypothetical Case

Figures 3b and 3c shows the tracer breakthrough curves (BTCs) simulated with the forward model of the simple hypothetical DFN depicted in Figure 3a. The assigned noise is not shown in the figures. The differences in the BTCs reflect the assumed anisotropy of the DFN, with smaller apertures of the high inclination fractures. The two upper injections from the left side did not produce any breakthroughs at the observation points. Observations where no breakthrough occurs frequently appear in the results of tomographic tracer tests, but they are often ignored in the inversion [Vasco and Datta-Gupta, 1999; Brauchler et al., 2013; Somogyvári et al., 2016]. If no breakthrough is observed within the simulated time, it is concluded that there is no (relevant) advective pathway leading from one point to the other. However, such findings are just as valuable as when tracer concentrations are measured and hence are also considered for misfit calculation here. The other four injections show very similar breakthrough behavior, with more spreading of those associated with longer travel times.

The used control parameters for the inversion procedure are summed up in Table 1. Note that the configuration of the inversion procedure does not allow for the exact reconstruction of the original DFN geometry. This geometry shown in Figure 3a is considered the hydraulically active part of a greater fracture network, which is expected to have a higher fracture intensity (0.7) with several inactive fractures that cannot be identified. Also, a different FLD is used for the inversion which is chosen according to the scale of the experiment [*Torabi and Berg*, 2011]. The used FLD follows a normal distribution with zero mean and variance of 25 m<sup>2</sup>. The discretization length of the DFNs is selected as 0.5 m. This level of discretization is capable of representing a DFN with the chosen parameters (FLD, fracture intensity), while keeping the simulation time of a tomographic experiment within a few seconds. The collected ensemble size was 30,000 realizations and the calculation took 48 h on an office PC (Intel<sup>®</sup> Core<sup>TM</sup> i7–6700k  $4 \times 4.0$  GHz). An additional crosscheck

<b>Table 1.</b> Parameters of the Inverse	Simple Model		Field-Based Model	
Fracture Set	Set 1	Set 2	Set 1	Set 2
Fracture inclination (°)	10	110	-12	58.9
Fracture aperture (mm)	0.3	0.2	0.15	0.1
Discretization length (m)	0.5		0.5	
Fracture intensity	0.7		0.4	
FLD – variance (m²)	25		72.25	
Likelihood variance	1.5		1.5	
$P_{add}/P_{del}/P_{shift}$	0.4/0.4/0.2		0.4/0.4/0.2	

with a doubled rjMCMC chain length (60,000) gave similar results, meaning that the smaller size is sufficiently large according to the given termination criteria.

The first few hundred accepted realizations in the sequence show a rapid decrease in the misfit (Figure 5a). This phase is the burn-in period where the realizations are still influenced by the used initial solution. This decrease stops after the first 1000 iterations. To completely eliminate the influence of this initial phase, the ensemble was built after the 2000th accepted realizations. The evolution of the misfits of the individual breakthrough curves (BTC) is presented in Figure 5b, normalized by the injection concentration of the tracer. The burn-in period serves as the adjustment of the concentration curves with very high initial misfits. After the initial period, misfits stabilize and fluctuate around small values. Often when there is an increase in RMS error at one BTC, this is compensated by a decrease at another.

For further result analysis, the Markov chain is thinned to 300 realizations. The quality of the individual fits on the BTCs is presented in Figure 5c. This figure serves as a first visual validation of the inversion results. "S#" represents the source number in the figures and "R#" denotes the observation points, according to the source receiver configuration shown in the bottom right corner. These breakthrough probability maps are generated similarly to the fracture probability map; rasterized BTCs are stacked together pixel-by-pixel. Fast BTCs show very good fits, while slower ones are slightly offset. Source-receiver combinations where no breakthrough was observed show perfect fits (see supporting information S1). This is because realizations where this is not reproduced, provide very high misfits and they get rejected immediately.

Figure 6 depicts the fracture probability map created from the result ensemble. The geometry of the hydraulically active fractures can be read from the high probability locations of the fracture probability map. As the most striking feature, the location of the main connecting fracture can be determined from the map: a high probability stripe connects the two wells. The most probable endpoints of this channel are located at the same locations relative to the sources and receivers as in the original model. The probability of the fractures connecting the source and receiver points with the aquifer is always 100% because they are kept fixed and not subject to inversion. The location of the two high-inclination fractures that connect these source-receiver fractures vertically is also visible in Figure 6 with high probability values. An additional low inclination fracture is proposed on the left side of the map between the upper two injection (or detection) points. The inversion is less sensitive to this area, probably because the two injection points nearby produced no breakthroughs. A large number of falsely identified fractures exist in the central area of the profile. Most of these fractures belong to the high-inclination fracture set 2. As this fracture set is less relevant for cross-well transport, it is more likely that some of such fractures freeze in and remain in many result realizations without any impact on the inversion. The additional low-inclination low-probability fractures provide alternative pathways to the transport in different realizations, results in equivalent BTCs. In order to run the inversion properly, higher fracture intensity was chosen than the synthetic reference, this is why many additional fractures exist within the individual DFN realizations. Most of these fractures are hydraulically inactive, and may disappear due to the updates (thus have small probabilities in the fracture probability map). However, they cannot be discarded during the inversion, as they provide possibilities for fracture addition and can become active in later iterations.

To separate the main DFN realization types within the ensemble, MDS is applied (Figure 7). The projection of the point cloud shows a nearly symmetric shape. Note that the circular shape is the result of the projection that tries to minimize distortions in the sample distances and has no further significance here. We

1944/973, 2017, 6, Downloaded from https://agupubs.onlinelibrary.wiley.com/doi/10.1002/2016WR020293 by Fak-Martin Luther Universitats, Wiley Online Library on [02/07/2024]. See the Terms and Conditions (https://onlinelibrary.wiley.com/etms-and-conditions) on Wiley Online Library for rules of use; OA articles are governed by the applicable Creative Commons

onlinelibrary.wiley.com/doi/10.1002/2016WR020293 by Fak-Martin Luther Universitats, Wiley Online Library on [02/07/2024]. See the Terms

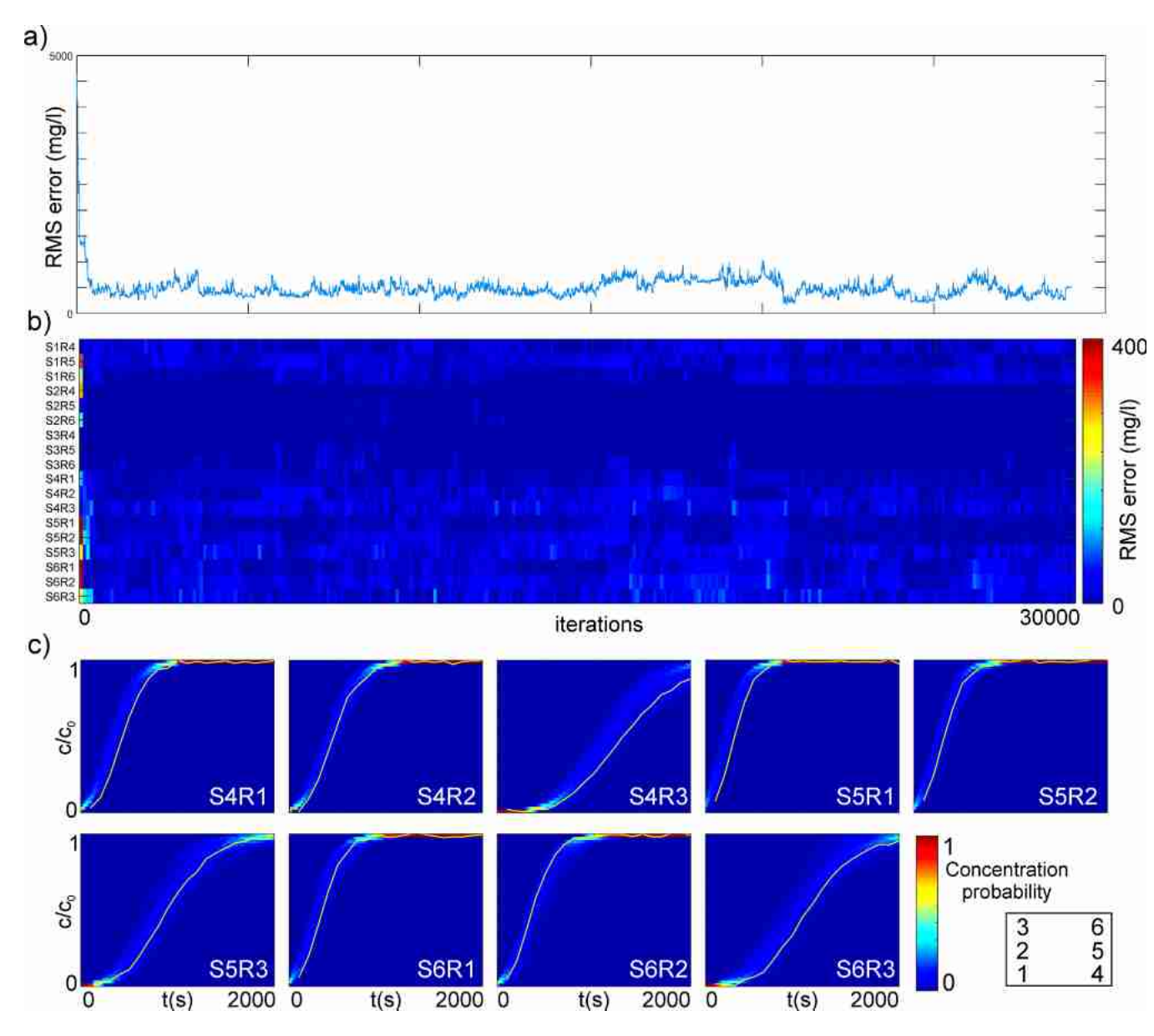


Figure 5. Inversion quality assessment. (a) RMS error of the accepted realizations through the Markov chain sequence. (b) Evolution of the misfits on the simulated breakthrough curves. (c) Fit quality of breakthrough curves of the second half of the experiment (reverse direction) in the whole ensemble (breakthrough probability maps). "S#" represents the source number, "R#" denotes the observation point (receiver) number, according to the source receiver configuration shown in the bottom right corner.

highlighted four different clusters of the MDS map (Figure 7a), originating from different phases of the inversion process (Figure 7b). Figure 7c shows the differences between the clusters by presenting the hydraulically active fractures from example realizations. The evolution of the different (but equally probable) DFN realizations can be seen by going through the clusters. The example of the first cluster is the most focused fracture network, with one choke-point on the right. This choke point remains in the second cluster, but the network to the left of it gets more spread. This spread continues in the next two clusters, reaching the right side of the domain as well. Yet in the fourth cluster, the fracture density in the center gets lower, making it somewhat more similar to the first cluster.

In Figure 7a, the colors of the points show that each cluster is built up from consecutive realizations. Ideally, after a large number of iterations, DFN realizations from the same clusters would not only contain samples from the same stage of convergence. This is because after many iterations, the points would start to mix on the MDS map as the inversion explores solutions again that have been reached earlier in the chain.

nditions) on Wiley Online Library for rules of use; OA articles are governed by the applicable Creative Commons

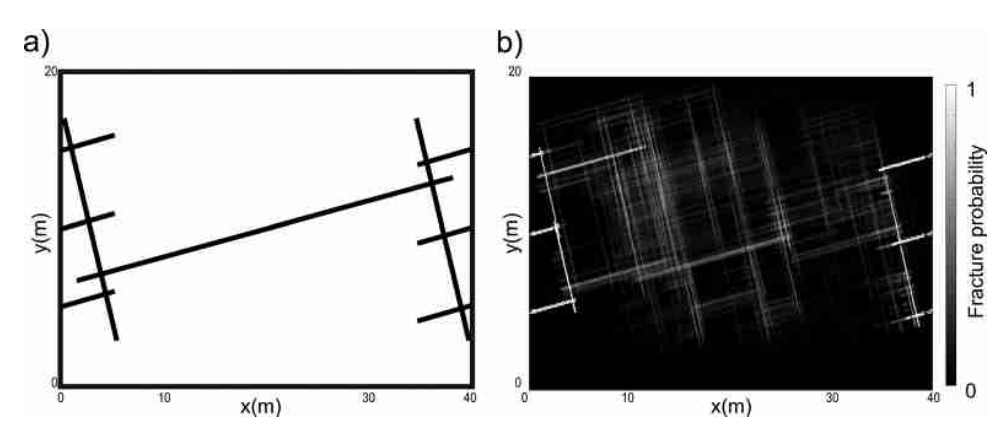
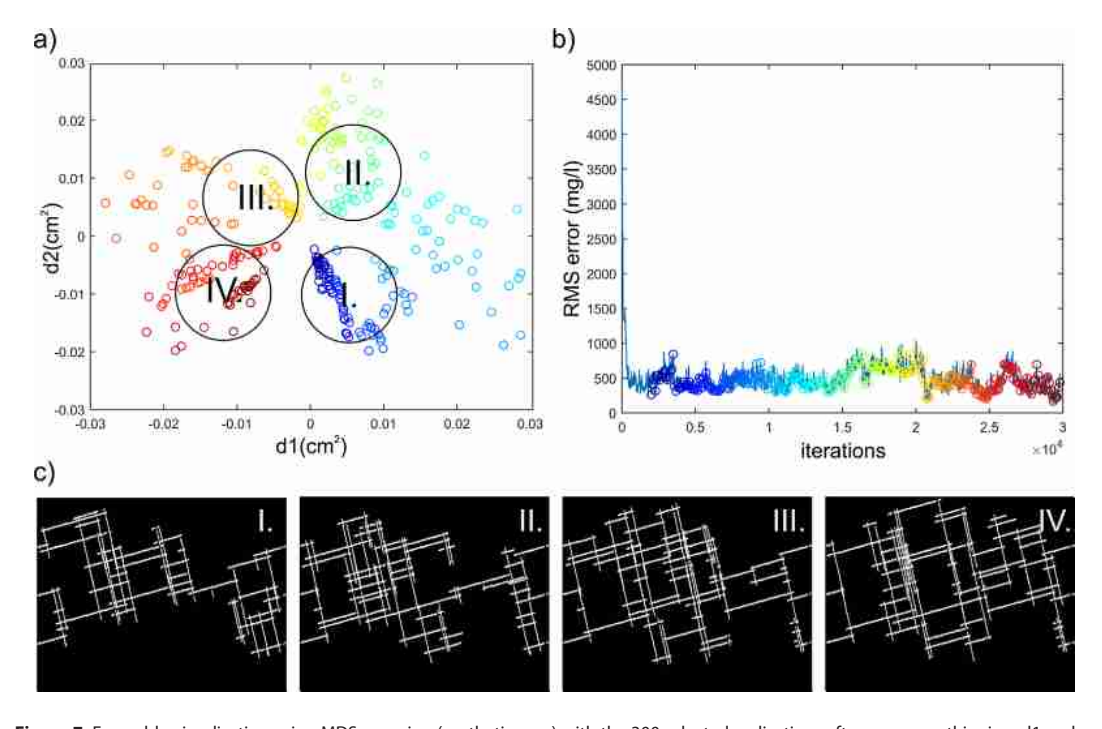


Figure 6. Inversion results of the synthetic scenario. (a) Synthetic fracture network model and (b) Inverted fracture probability map generated from 300 DEN realizations

Although the latest realizations started to become similar to the first ones in our sequence, further analysis of the longer (doubled) sequence showed that in fact no mixing had started to develop yet.

It is interesting to compare the example realizations (Figure 7c) of the clusters to the final fracture probability map (Figure 7a). It is obvious that these realizations contain information of the final result, but none of them is capable of representing the original fracture network alone. No big difference in the BTCs of the different clusters is visible, since the fit of the BTCs show minimal variance throughout the full ensemble (see Figure 5c). The variations in the misfit values are mainly caused by the slowest breakthrough curves, which are most affected by the differences between them, while the quickest transport routes are constant.

Changes in the geometry which modify the fastest transport pathways would alter multiple breakthroughs at the same time. This type of changes drives the burn-in period of the rjMCMC sequence, where the general transport pattern is adjusted to the observations. In the converged phase of the algorithm, these updates are rare, as they only get accepted if they do not make a very large increase in the misfits. This



**Figure 7.** Ensemble visualization using MDS mapping (synthetic case) with the 300 selected realizations after sequence thinning. d1 and d2 are the virtual dimensions of the MDS projection. (a) MDS map and identified clusters, (b) Convergence of the inversion with selected realizations, and (c) DFN examples from the identified clusters.

1944/7973, 2017, 6, Downloaded from https://agupubs.onlinelibrary.wiley.com/doi/10.1002201 6WR020293 by Fak-Martin Luther Universitats, Wiley Online Library on [02/07/2024]. See the Terms and Conditions (https://onlinelibrary.wiley.com

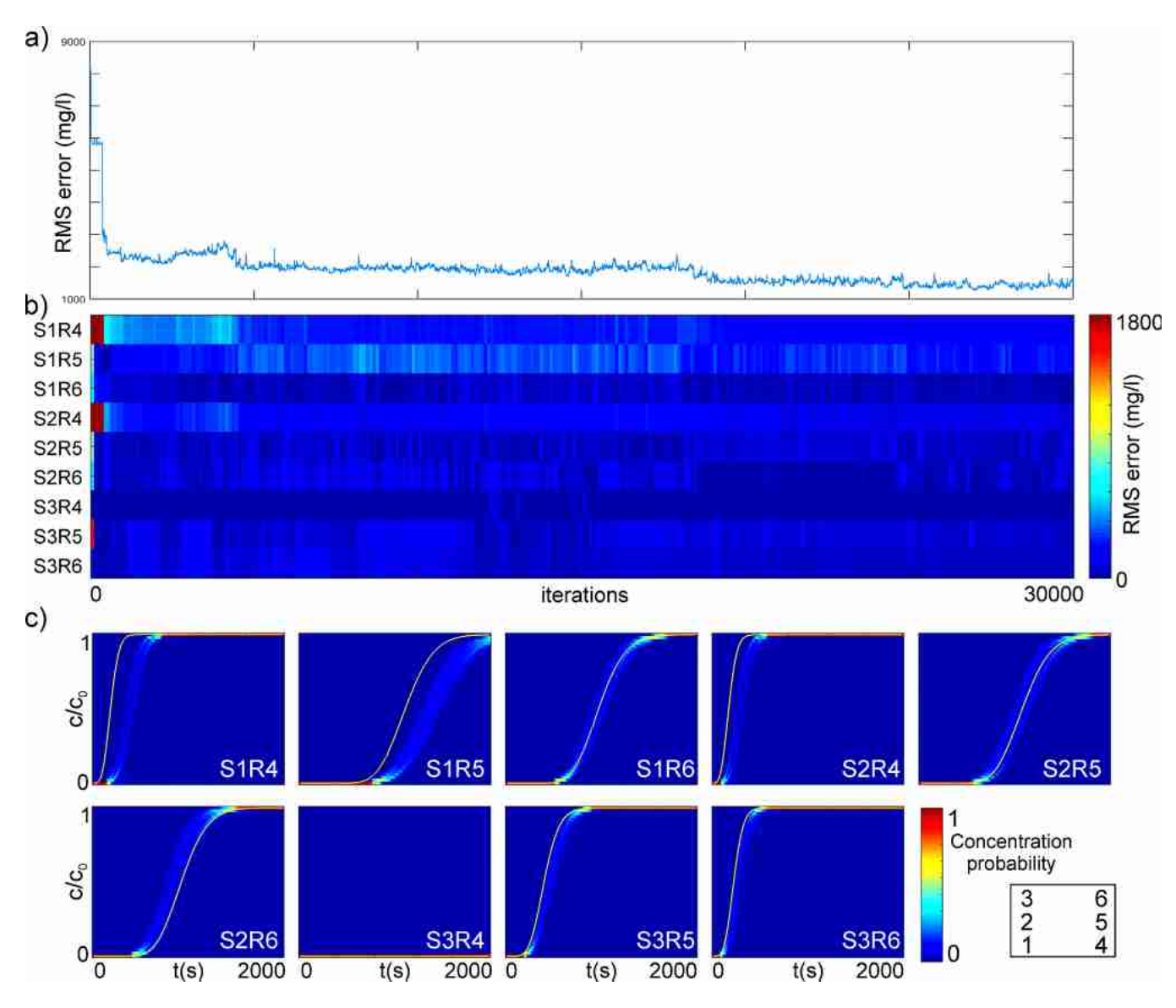


Figure 8. Inversion quality assessment of the outcrop-based scenario. (a) RMS error of the accepted realizations through the Markov chain sequence. (b) Evolution of the misfits on the simulated BTCs. (c) Fit quality of breakthrough curves in the whole ensemble (breakthrough probability maps). "S#" represents the source number, "R#" denotes the observation point (receiver) number, according to the source receiver configuration shown in the bottom right corner.

explains why the fracture probability map shows only one main transport pathway and not multiple different ones.

Due to the highly discretized behavior, the risk of the algorithm to become trapped in a local minimum is higher than in rjMCMC studies developed to interpret continuous problems [e.g., *Bodin and Sambridge*, 2009; *Jiménez et al.*, 2016]. The discrete geometry strongly limits the freedom of updates since, as always, a limited number of possible updates are available. Using higher likelihood variance, the inversion can escape from most of the local minimums, but posteriors with highly bi- or multimodal behavior could require multiple model runs for complete sampling. In the presented scenarios, the inversion always converged to similar solutions, independent from the initial realization.

### 5.2. Outcrop-Based Case

In the following, we present the results for the more complex outcrop-based fracture network (Figure 4). The statistical properties of the outcrop (Figures 4b–4d) are taken to configure the search procedure (Table 1). The fracture intensity of the middle part of the outcrop is used for the inversion (0.4). A truncated

and-conditions) on Wiley Online Library for rules of use; OA articles are governed by the applicable Creative Commons

1944/7973, 2017, 6, Downloaded from https://agupubs.onlinelibrary.wiley.com/doi/10.10022016WR020293 by Fak-Martin Luther Universitats, Wiley Online Library on [02/07/2024]. See the Terms and Conditions (https://onlinelibrary.wiley.com/

normal distribution is determined to approximate the FLD of the network, with the smallest allowed fracture size of 1 m. With 0 m mean and 72.25  $m^2$  variance, this approximates the distribution of the smaller fractures in the investigated fracture network well. Very long fractures are only expected to be drawn as outliers from the used FLD. Thus, very long fractures of the outcrop should be mainly built up by shorter segments in the generated DFN realizations. The discretization length of the DFNs is 0.5 m. The inclinations of the fracture sets in the inverse model are defined after inspecting the fracture inclination distribution of the outcrop shown on Figure 4d, where two dominant fracture inclinations exist. The two used inclinations are  $-12^{\circ}$  and  $59^{\circ}$ , respectively. Note that due to this restriction, as well as due to the approximate settings for fracture intensity and FLD, the investigated DFN geometry can only be approximated by the inversion and not exactly reproduced.

Again, similar to the hypothetical case, 30,000 realizations were collected for the ensemble and 2000 realizations were discarded as burn-in phase (Figure 8a). The converged RMS error values are higher than in the hypothetical case, because the experimental times were longer and the BTCs consisted of (five times) more data points. As a consequence, the misfit values of the individual BTCs are higher for this case (Figures 8b and 8c). At early breakthroughs (e.g., S1R4 or S2R4), the reconstructed breakthroughs are late. In comparison, latter breakthroughs show good fits except of S1R5. This one is the latest among all the BTCs, and it also shows the weakest fit (200s late) with the largest variance. The used misfit criterion is most sensitive to the elongated BTCs, where the increase in concentration spans through the whole time interval (e.g., S1R6, S2R5). Thus, elongated BTCs are the main drivers of the inversion procedure. For example, comparing S2R6 to S3R5, the fit of S3R5 is better (Figure 8c) but the misfits are in the same range (Figure 8b).

The DFN results of the inversion are shown by Figure 9. A main feature of the original fracture network is that it is split into two loosely connected fractured areas, an upper and a lower one. This is visible also in the fracture probability map (Figure 9b). Some nonfractured areas of the domain are well reproduced and the strongly

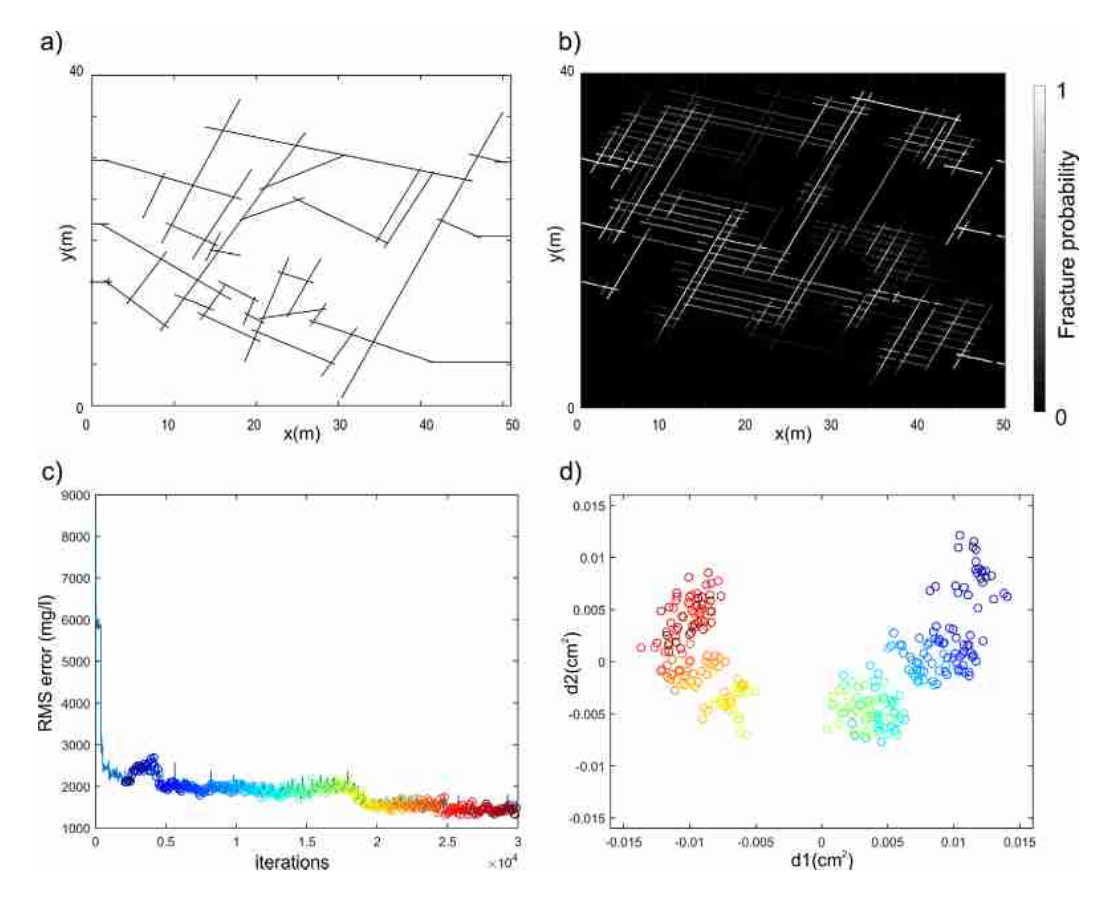


Figure 9. Inversion results of the outcrop-based scenario. (a) Outcrop-based fracture network model, (b) fracture probability map of the reconstruction, (c) convergence rate of rjMCMC (with the selected samples marked), and (d) MDS mapping of the ensemble subset.

use; OA articles are governed by the applicable Creative Commons

fractured area in the bottom left quarter of the original domain is recognizable in the fracture probability map. Overall, the main transport pathways are easy to identify from Figure 9b, but the individual fractures often appear multiplied. A closer look reveals that fracture set 2 consists of multiple doubled fractures, while fracture set 1 has multiple quadrupled fractures. This is the effect of discretization and limited sensitivity of slightly shifted fractures that cause minor change in the BTCs. In studies using continuous models, the same effect appears as the smoothness of the final result [Bodin and Sambridge, 2009; Jiménez et al., 2016].

The used discretization length was chosen to support fast computations. Since the value of 0.5 m is larger than the smallest fracture spacing in the outcrop and the distance of the two wells are 50 m, it is considered small enough for the DFN reconstruction. It is also smaller than the shortest mapped fractures of the investigated fracture network. Under field conditions, the discretization level can be chosen based on the observed spacing of the fractures. Using a small discretization length improves the resolution of the reconstruction and it improves the fracture length estimation since the used FLD is also discrete. However, the associated increase in degrees of freedom for fracture calibration means higher computation times and hampers discrete identification of fractures. Coarser discretization levels may cause a neglect of relevant small-scale features and could strongly limit the number of possible solutions delivered by the inversion. Long fractures are more likely to be reconstructed, but with less accurate fracture length estimation.

The MDS map (Figure 9d) shows that the differences between the DFN realizations are significantly smaller than in the hypothetical case. This means that the realizations are more similar to each other and the solution provides less equivalent tracer pathways than the hypothetical case. The point cloud is more mixed even though it shows a general clockwise trend, but the points do not follow each other sequentially. This could be an indicator on the completeness of the sampling, but also can be an effect of the small differences in the DFN geometries.

### 6. Conclusions

Fracture systems in hard rocks are commonly described by statistical information on orientation, spacing, and intensity of fracture sets. This information is used to generate candidates of discrete fracture networks (DFNs) that describe the hydrogeological conditions in the field. There is still a lack of techniques that allow flexible calibration of DFNs to data from spatially resolved field measurements, which were obtained from geophysical, hydrogeophysical, or hydrogeological investigations. A main hurdle is the often large number of tuning parameters which is tied to the number of fractures used in the model. The number of fractures, however, is not known a priori. This is tackled in this study by introducing a transdimensional inversion procedure (rjMCMC) that adjusts geometrical values and fracture numbers during the calibration. By processing both the statistical description of the fractured rock and data from field experiments, a new concept of DFN model calibration is developed.

The presented implementation of rjMCMC automatically develops a connected fracture network by sequentially creating, deleting, and moving fracture segments in space. Its potential is evaluated with a simple synthetic and a field-derived fracture network, which are both reconstructed based on conservative tracer tomography experiments. As a result, an ensemble of DFN realizations is obtained that reveals highly probable locations of those fractures relevant for tracer transport. We introduced fracture probability maps, extracted from the ensemble representative realizations based on clustering and multidimensional scaling. These results can also be exploited for case-specific production probability assessment or risk assessment.

By comparison to the original DFNs, it was demonstrated that major geometrical features could be identified. It is also revealed that often equally probable geometries exist and adjacent fractures yield similar results. Accordingly, small-scale variations could not be resolved. Ideally local high fracture intensities appear in the fracture probability map as densely spaced active fractures with high probabilities. The main control parameter for the obtained fracture resolution is the discretization, the role of which needs to be further explored in sensitivity analyses. A logical next step is to include additional data from complementary field tests, such as from near-surface geophysics which could reduce the nonunique behavior of the results. As the presented Bayesian inversion framework allows joint consideration of different types of data, DFN reconstruction could be improved when compared with using only tracer data as in the presented work. There is also room for improvement by refining the misfit calculation of tracer BTCs, which is based on standard RMS error computation. For example, a weighted error calculation may be applied to adjust the

1944/973, 2017, 6, Downloaded from https://agupubs.onlinelibrary.wiley.com/doi/10.1002/2016WR020293 by Fak-Martin Luther Universitats, Wiley Online Library on [02/07/2024]. See the Terms and Conditions (https://onlinelibrary.wiley.com/term

significance of different source receiver combinations, or to control the importance of early, normal, and late breakthroughs. Another possible option is to use selected tracer travel times instead of direct BTC comparison.

In future work, we will also consider three-dimensional DFN reconstruction and calibration of the fracture apertures. This will require a higher information density from (simulated) field experiments, or tighter constraints to localize sensitive (or active) fractures. The presented inversion framework is not limited to 2-D, but an additional dimension will raise the computational time for the forward model and it will reduce the convergence rate of the Markov chain. Note that for the presented cross-well sections, the forward model was executed in a few seconds. So even with an additional dimension, and when simulating alternative transport behavior (e.g., retardation of tracer), computation times will be in a feasible range. Aside from this, promising advanced rjMCMC schemes (e.g., delayed rejection) [Bodin and Sambridge, 2009] and highperformance computers have not been considered yet. Computational performance may be improved by simulating shorter Markov chains in parallel and handling the results together. As with discarding realizations of the burn-in phase, the influence of the used initial solution can be minimized and sequences generated with the same control parameters may be handled together. However, during the development of the method so far, we have focused on optimization for single chain performance. In the current version, the implemented algorithm runs best on high single thread performance CPUs. Involving the fracture aperture in the inversion would greatly reduce the convergence rate and increase the instability of the inverse problem. Thus inverting apertures will require additional constrains on the model parameters, or the involvement of additional data in the inversion. Although the proposed methodology is presented for conservative tracer tomography, other types of experiments, such as hydraulic tomography or alternative hydrogeophysical investigations can be interpreted.

#### Acknowledgments

This work was supported by the Swiss National Science Foundation under grant number 200021\_149128. We thank Walter Illman and two anonymous reviewers for the constructive comments and Rachael Colldeweih for language corrections. All data are available by contacting the corresponding author (mark. somogyvari@erdw.ethz.ch).

### References

- Aster, R. C., B. Borchers, and C. H. Thurber (2013), *Parameter Estimation and Inverse Problems*, Academic, Oxford, U. K. Baghbanan, A., and L. Jing (2007), Hydraulic properties of fractured rock masses with correlated fracture length and aperture, *Int. J. Rock Mech. Min. Sci.*, 44(5), 704–719, doi:10.1016/j.ijrmms.2006.11.001.
- Berg, S. J., and W. A. Illman (2011), Three-dimensional transient hydraulic tomography in a highly heterogeneous glaciofluvial aquiferaquitard system, *Water Resour. Res.*, 47, W10507, doi:10.1029/2011WR010616.
- Berkowitz, B. (2002), Characterizing flow and transport in fractured geological media: A review, *Adv. Water Resour.*, 25(8–12), 861–884, doi: 10.1016/S0309-1708(02)00042-8.
- Bodin, T., and M. Sambridge (2009), Seismic tomography with the reversible jump algorithm, *Geophys. J. Int.*, 178(3), 1411–1436, doi: 10.1111/j.1365-246X.2009.04226.x.
- Borg, I., and P. J. F. Groenen (2005), Modern Multidimensional Scaling: Theory and Applications, Springer, New York.
- Bossart, P., and M. Mazurek (1991), Structural Geology and Water Flow-Paths in the Migration Shear Zone, technical report, Nagra, Wettingen, Switzerland.
- Bour, O., and P. Davy (1997), Connectivity of random fault networks following a power law fault length distribution, *Water Resour. Res.*, 33(7), 1567–1583, doi:10.1029/96WR00433.
- Brauchler, R., R. Liedl, and P. Dietrich (2003), A travel time based hydraulic tomographic approach, *Water Resour. Res.*, 39(12), 1370, doi: 10.1029/2003WR002262.
- Brauchler, R., G. Böhm, C. Leven, P. Dietrich, and M. Sauter (2013), A laboratory study of tracer tomography, *Hydrogeol. J.*, 21(6), 1265–1274, doi:10.1007/s10040-013-1006-z.
- Caers, J., K. Park, and C. Scheidt (2010), Modeling uncertainty of complex earth systems in metric space, in *Handbook of Geomathematics*, edited by W. Freeden, M. Z. Nashed, and T. Sonar, pp. 865–889, Springer, Berlin.
- Castagna, M., M. W. Becker, and A. Bellin (2011), Joint estimation of transmissivity and storativity in a bedrock fracture, *Water Resour. Res.*, 47, W09504, doi:10.1029/2010WR009262.
- Darcel, C., O. Bour, P. Davy, and J. R. de Dreuzy (2003), Connectivity properties of two-dimensional fracture networks with stochastic fractal correlation, *Water Resour. Res.*, 39(10), 1272, doi:10.1029/2002WR001628.
- Datta-Gupta, A., D. W. Vasco, and J. C.. Long (1995), Detailed Characterization of a Fractured Limestone Formation by Use of Stochastic Inverse Approaches, SPE Form. Eval., 10(3), 133–140, doi:10.2118/27744-PA.
- Day-Lewis, F. D., P. A. Hsieh, and S. M. Gorelick (2000), Identifying fracture-zone geometry using simulated annealing and hydraulic-connection data, *Water Resour. Res.*, 36(7), 1707–1721, doi:10.1029/2000WR900073.
- de Dreuzy, J.-R., P. Davy, and O. Bour (2002), Hydraulic properties of two-dimensional random fracture networks following power law distributions of length and aperture, *Water Resour. Res.*, 38(12), 1276, doi:10.1029/2001WR001009.
- Djibrilla Saley, A., A. Jardani, A. Soueid Ahmed, A. Raphael, and J. P. Dupont (2016), Hamiltonian Monte Carlo algorithm for the characterization of hydraulic conductivity from the heat tracing data, Adv. Water Resour., 97, 120–129, doi:10.1016/j.advwatres.2016.09.004.
- Dorn, C., N. Linde, T. Le Borgne, O. Bour, and J. R. de Dreuzy (2013), Conditioning of stochastic 3-D fracture networks to hydrological and geophysical data, *Adv. Water Resour.*, 62(PA), 79–89, doi:10.1016/j.advwatres.2013.10.005.
- Doro, K. O., O. a Cirpka, and C. Leven (2015), Tracer tomography: Design concepts and field experiments using heat as a tracer, *Groundwater*, 53(S1), 139–148, doi:10.1111/gwat.12299.
- Frampton, A., and V. Cvetkovic (2010), Inference of field-scale fracture transmissivities in crystalline rock using flow log measurements, *Water Resour. Res.*, 46, W11502, doi:10.1029/2009WR008367.

nditions) on Wiley Online Library for rules of use; OA articles are governed by the applicable Creative Commons

onlinelibrary.wiley.com/doi/10.1002/2016WR020293 by Fak-Martin Luther Universitats, Wiley Online Library on [02/07/2024]. See the Terms

- Franssen, H. J. W. M. H., and J. J. Gómez-Hernández (2002), 3D inverse modelling of groundwater flow at a fractured site using a stochastic continuum model with multiple statistical populations, *Stochastic Environ. Res. Risk Assess.*, 16(2), 155–174, doi:10.1007/s00477-002-0091-7
- Gelman, A., J. B. Carlin, H. S. Stern, and D. B. Rubin (2004), Bayesian Data Analysis, CRC Press, Boca Raton, Fla.
- Geyer, C. (2011), Introduction to Markov Chain Monte Carlo, in *Handbook of Markov Chain Monte Carlo*, vol. 20116022, edited by S. Brooks et al., p. 45, Chapman and Hall, Boca Raton, Fla.
- Green, P. J. (1995), Reversible jump Markov chain monte carlo computation and Bayesian model determination, *Biometrika*, 82(4), 711–732, doi:10.1093/biomet/82.4.711.
- Hao, Y., T.-C. J. Yeh, J. Xiang, W. A. Illman, K. Ando, K.-C. Hsu, and C.-H. Lee (2008), Hydraulic tomography for detecting fracture zone connectivity, Ground Water, 46(2), 183–192, doi:10.1111/j.1745-6584.2007.00388.x.
- Hestir, K., S. J. Martel, S. Vail, J. Long, P. D'Onfro, and W. D. Rizer (1998), Inverse hydrologic modeling using stochastic growth algorithms, Water Resour. Res., 34(12), 3335–3347, doi:10.1029/98WR01549.
- Hestir, K., S. J. Martel, J. Yang, J. P. Evans, J. O. S. Long, P. D'Onfro, and W. D. Rizer (2001), Use of conditional simulation, mechanical theory, and field observations to characterize the structure of faults and fracture networks, in *Flow and Transport through Unsaturated Fractured Rock*, edited by D. D. Evans, T. J. Nicholson and T. C. Rasmussen, pp. 61–73, AGU, Washington, D. C., doi:10.1029/GM042p0061.
- Hu, L., P. Bayer, P. Alt-Epping, A. Tatomir, M. Sauter, and R. Brauchler (2015), Time-lapse pressure tomography for characterizing CO2 plume evolution in a deep saline aquifer, *Int. J. Greenhouse Gas Control*, 39, 91–106, doi:10.1016/j.ijggc.2015.04.013.
- Illman, W. A. (2014), Hydraulic tomography offers improved imaging of heterogeneity in fractured rocks, *Groundwater*, 52(5), 659–684, doi: 10.1111/gwat.12119.
- Illman, W. A., and S. P. Neuman (2003), Steady-state analysis of cross-hole pneumatic injection tests in unsaturated fractured tuff, J. Hydrol., 281(1–2), 36–54. doi:10.1016/S0022-1694(03)00199-9.
- Illman, W. A., X. Liu, S. Takeuchi, T.-C. J. Yeh, K. Ando, and H. Saegusa (2009), Hydraulic tomography in fractured granite: Mizunami Underground Research site, Japan, *Water Resour. Res.*, 45, W01406, doi:10.1029/2007WR006715.
- Illman, W. A., S. J. Berg, X. Liu, and A. Massi (2010), Hydraulic/partitioning tracer tomography for DNAPL source zone characterization: Small-scale sandbox experiments, *Environ. Sci. Technol.*, 44(22), 8609–8614, doi:10.1021/es101654j.
- Illman, W. A., S. J. Berg, and Z. Zhao (2015), Should hydraulic tomography data be interpreted using geostatistical inverse modeling? A laboratory sandbox investigation, *Water Resour. Res.*, 51, 3219–3237, doi:10.1002/2014WR016552.
- Jalali, M. (2013), Thermo-hydro-mechanical behavior of conductive fractures using a hybrid finite difference: Displacement discontinuity method, p. 187, Nat. Sci. and Eng. Counc. (NSERC) of Canada, Univ. of Waterloo, Waterloo, Canada, doi:http://hdl.handle.net/10012/7642.
- Jang, I. S., J. M. Kang, and C. H. Park (2008), Inverse fracture model integrating fracture statistics and well-testing data, Energy Sour. Part A Recover. Util. Environ. Eff., 30(18), 1677–1688, doi:10.1080/15567030802087510.
- Jiménez, S., G. Mariethoz, R. Brauchler, and P. Bayer (2016), Smart pilot points using reversible-jump Markov-chain Monte Carlo, Water Resour. Res., 3966–3983, doi:10.1002/2015WR017922.
- Klepikova, M. V., T. Le Borgne, O. Bour, K. Gallagher, R. Hochreutener, and N. Lavenant (2014), Passive temperature tomography experiments to characterize transmissivity and connectivity of preferential flow paths in fractured media, *J. Hydrol.*, *512*, 549–562, doi: 10.1016/j.jhydrol.2014.03.018.
- Le Borgne, T. et al. (2007), Comparison of alternative methodologies for identifying and characterizing preferential flow paths in heterogeneous aquifers, J. Hydrol., 345(3–4), 134–148, doi:10.1016/j.jhydrol.2007.07.007.
- Le Goc, R., J.-R. de Dreuzy, and P. Davy (2010), An inverse problem methodology to identify flow channels in fractured media using synthetic steady-state head and geometrical data, *Adv. Water Resour.*, 33(7), 782–800, doi:10.1016/j.advwatres.2010.04.011.
- La Pointe, P. R. (1988), A method to characterize fracture density and connectivity through fractal geometry, Int. J. Rock Mech. Min. Sci. Geomech. Abstr., 25(6), 421–429, doi:10.1016/0148-9062(88)90982-5.
- Li, Z. Y., J. H. Zhao, X. H. Qiao, and Y. X. Zhang (2014), An automated approach for conditioning discrete fracture network modelling to in situ measurements, Aust. J. Earth Sci., 61(5), 755–763, doi:10.1080/08120099.2014.920726.
- Long, J. C. S., J. S. Remer, C. R. Wilson, and P. A. Witherspoon (1982), Porous media equivalents for networks of discontinuous fractures, *Water Resour. Res.*, 18(3), 645–658, doi:10.1029/WR018i003p00645.
- Mardia, K. V., V. B. Nyirongo, A. N. Walder, C. Xu, P. A. Dowd, R. J. Fowell, and J. T. Kent (2007), Markov Chain Monte Carlo implementation of rock fracture modelling, *Math. Geol.*, 39(4), 355–381, doi:10.1007/s11004-007-9099-3.
- Martinez-Landa, L., and J. Carrera (2006), A methodology to interpret cross-hole tests in a granite block, *J. Hydrol.*, 325(1–4), 222–240, doi: 10.1016/j.jhydrol.2005.10.017.
- Mauldon, A. D., K. Karasaki, S. J. Martel, J. C. S. Long, M. Landsfeld, A. Mensch, and S. Vomvoris (1993), An inverse technique for developing models for fluid flow in fracture systems using simulated annealing, *Water Resour. Res.*, 29(11), 3775–3789, doi:10.1029/93WR00664.
- Meier, P. M., A. Medina, and J. Carrera (2001), Geostatistical inversion of cross-hole pumping tests for identifying preferential flow channels within a shear zone, *Ground Water*, 39(1), 10–17, doi:10.1111/j.1745-6584.2001.tb00346.x.
- Menke, W. (1984), Geophysical Data Analysis: Discrete Inverse Theory, Academic, New York.
- Mondal, A., Y. Efendiev, B. Mallick, and A. Datta-Gupta (2010), Bayesian uncertainty quantification for flows in heterogeneous porous media using reversible jump Markov chain Monte Carlo methods, *Adv. Water Resour.*, 33(3), 241–256, doi:10.1016/j.advwatres.2009.10.010.
- Neretnieks, I. (1980), Diffusion in the rock matrix: An important factor in radionuclide retardation?, J. Geophys. Res., 85(B8), 4379–4397, doi: 10.1029/JB085iB08p04379.
- Neuman, S. P. (1988), Stochastic continuum representation of fractured rock permeability as an alternative to the rev and fracture network concepts, in *Groundwater Flow and Quality Modelling*, pp. 331–362, Springer, Dordrecht, Netherlands.
- Neuman, S. P. (2005), Trends, prospects and challenges in quantifying flow and transport through fractured rocks, Hydrogeol. J., 13(1), 124–147, doi:10.1007/s10040-004-0397-2.
- Ni, C. F., and T. C. J. Yeh (2008), Stochastic inversion of pneumatic cross-hole tests and barometric pressure fluctuations in heterogeneous unsaturated formations, *Adv. Water Resour.*, 31(12), 1708–1718, doi:10.1016/j.advwatres.2008.08.007.
- Niven, E. B., and C. V. Deutsch (2012), Non-random discrete fracture network modeling, in *Quantitative Geology and Geostatistics*, vol. 17, edited by P. Abrahamsen, R. Hauge, and O. Kolbjørnsen, pp. 275–286, Springer, Dordrecht, Netherlands.
- Noetinger, B., D. Roubinet, A. Russian, T. Le Borgne, F. Delay, M. Dentz, J.-R. de Dreuzy, and P. Gouze (2016), Random walk methods for modeling hydrodynamic transport in porous and fractured media from pore to reservoir scale, *Transp. Porous Media*, 115(2), 345–385, doi:10.1007/s11242-016-0693-z.
- Paradis, D., E. Gloaguen, R. Lefebvre, and B. Giroux (2015), Resolution analysis of tomographic slug test head data: Two-dimensional radial case, *Water Resour. Res.*, 51, 2356–2376, doi:10.1002/2013WR014785.

use; OA articles are governed by the applicable Creative Comm

onlinelibrary.wiley.com/doi/10.1002/2016WR020293 by Fak-Martin Luther Universitats, Wiley Online Library on [02/07/2024]. See the Terms

- Sahimi, M. (2011), Flow and Transport in Porous Media and Fractured Rock: From Classical Methods to Modern Approaches, John Wiley, Hoboken, N. J.
- Sambridge, M., T. Bodin, K. Gallagher, and H. Tkalcic (2012), Transdimensional inference in the geosciences, *Philos. Trans. R. Soc. A*, 371(1984), 20110547–20110547, doi:10.1098/rsta.2011.0547.
- Schöniger, A., W. Nowak, and H.-J. Hendricks Franssen (2012), Parameter estimation by ensemble Kalman filters with transformed data: Approach and application to hydraulic tomography, *Water Resour. Res.*, 48, W04502, doi:10.1029/2011WR010462.
- Sharmeen, R., W. A. Illman, S. J. Berg, T.-C. J. Yeh, Y.-J. Park, E. A. Sudicky, and K. Ando (2012), Transient hydraulic tomography in a fractured dolostone: Laboratory rock block experiments, *Water Resour. Res.*, 48, W10532, doi:10.1029/2012WR012216.
- Somogyvári, M., P. Bayer, and R. Brauchler (2016), Travel-time-based thermal tracer tomography, *Hydrol. Earth Syst. Sci.*, 20(5), 1885–1901, doi:10.5194/hess-20-1885-2016.
- Torabi, A., and S. S. Berg (2011), Scaling of fault attributes: A review, *Mar. Pet. Geol.*, 28(8), 1444–1460, doi:10.1016/j.marpetgeo.2011.04.003. Valley, B. C. (2007), The relation between natural fracturing and stress heterogeneities in deep-seated crystalline rocks at Soultz-sous-Forets (France), 17385, 260 p., ETH Reprozentrale Hönggerberg, Zürich. [Available at http://dx.doi.org/10.3929/ethz-a-005562794.]
- Vasco, D. W., and A. Datta-Gupta (1999), Asymptotic solutions for solute transport: A formalism for tracer tomography, *Water Resour. Res.*, 35(1), 1–16, doi:10.1029/98WR02742.
- Vesselinov, V. V, S. P. Neuman, and W. A. Illman (2001a), Three-dimensional numerical inversion of pneumatic cross-hole tests in unsaturated fractured tuff: 1. Methodology and borehole effects, Water Resour. Res., 37(12), 3001–3017, doi:10.1029/2000WR000133.
- Vesselinov, V. V., S. P. Neuman, and W. A. Illman (2001b), Three-dimensional numerical inversion of pneumatic cross-hole tests in unsaturated fractured tuff: 2. Equivalent parameters, high-resolution stochastic imaging and scale effects, *Water Resour. Res.*, 37(12), 3019–3041. doi:10.1029/2000WR000135.
- Yeh, T.-C. J., M. Jin, and S. Hanna (1996), An Iterative Stochastic Inverse Method: Conditional Effective Transmissivity and Hydraulic Head Fields. Water Resour. Res., 32(1), 85–92. doi:10.1029/95WR02869.
- Zha, Y., T.-C. J. Yeh, W. A. Illman, T. Tanaka, P. Bruines, H. Onoe, and H. Saegusa (2015), What does hydraulic tomography tell us about fractured geological media? A field study and synthetic experiments, *J. Hydrol.*, *531*, 17–30, doi:10.1016/j.jhydrol.2015.06.013.
- Zha, Y., T.-C. J. Yeh, W. A. Illman, T. Tanaka, P. Bruines, H. Onoe, H. Saegusa, D. Mao, S. Takeuchi, and J.-C. Wen (2016), An application of hydraulic tomography to a large-scale fractured granite site, Mizunami, Japan, *Groundwater*, 54(6), 1–12, doi:10.1111/gwat.12421.
- Zhou, Y., D. Lim, F. Cupola, and M. Cardiff (2016), Aquifer imaging with pressure waves-Evaluation of low-impact characterization through sandbox experiments, *Water Resour. Res.*, *52*, 2141–2156, doi:10.1002/2015WR017751.
- Ziegler, M., S. Loew, and J. R. Moore (2013), Distribution and inferred age of exfoliation joints in the Aar Granite of the central Swiss Alps and relationship to Quaternary landscape evolution, *Geomorphology*, 201, 344–362, doi:10.1016/j.geomorph.2013.07.010.
- Ziegler, M., S. Loew, and D. Bahat (2014), Growth of exfoliation joints and near-surface stress orientations inferred from fractographic markings observed in the upper Aar valley (Swiss Alps), *Tectonophysics*, 626, 1–20, doi:10.1016/j.tecto.2014.03.017.
- Ziegler, M., B. Valley, and K. F. Evans (2015), Characterisation of natural fractures an fracture zones of the basel EGS reservoir inferred from geophysical logging of the Basel-1 well, in World Geothermal Congress 19–25 Apr, Melbourne, Australia, pp. 19–25, Int. Geotherm. Assoc., Bochum.